

CNT-based electro-responsive shape memory functionalized 3D printed nanocomposites for liquid sensors

Xue Wan^a, Fenghua Zhang^a, Yanju Liu^b, Jinsong Leng^{a,*}

^a National Key Laboratory of Science and Technology on Advanced Composites in Special Environments, Harbin Institute of Technology, Harbin, 150080, People's Republic of China

^b Department of Astronautical Science and Mechanics, Harbin Institute of Technology, Harbin, 150001, People's Republic of China

ARTICLE INFO

Article history:

Received 2 June 2019

Received in revised form

29 July 2019

Accepted 13 August 2019

Available online 13 August 2019

ABSTRACT

3D printing of conductive polymer nanocomposites, which combines the electrical conductivity of nanofillers with customer-designed geometries, is promising for various sensors. However, the single shape of sensors restricts their environmental adaptability if the detecting environment changes. Herein, 3D and 4D printing of poly (D,L-lactide-co-trimethylene carbonate) (PLMC)/CNT nanocomposites with electro-responsive shape-changing capability was achieved by direct ink writing (DIW). The rheological and solvent evaporation capabilities of PLMC/CNT ink were modulated to make it printable. Electrical, mechanical, thermal and shape memory properties were investigated and various structures from micro to macro were constructed. The printed structure showed excellent shape-changing behavior under 25 V within 16 s. Then UV photoinitiators were introduced to trigger hydrogen abstraction reaction to make PLMC chains form cross-linking networks. The modified composite ink was printed into shape-changing liquid sensors. The influence of three solvents and layer thickness on liquid sensitivity was compared. The shape-changing capability helped the sensor maintain a high precision for liquid detection. The sensor in its original, deformed and recovered shape showed similar changing trend of resistance and exhibited excellent repeatability. We envision wide environmental adaptability of using the shape-changing sensor for detecting leakage of various solvents in varying environment.

© 2019 Elsevier Ltd. All rights reserved.

1. Introduction

Conductive polymer nanocomposites with carbon nanotubes (CNT) [1,2], graphene [3], carbon grease [4] and silver nanoparticles [5], are multifunctional materials due to their high strength, electrical conductivity and thermal stability. With the development of 3D printing, multifunctional nanocomposites could be printed into complex customer-designed 3D geometries. The printed conductive nanocomposites have potential in various sensors, such as strain sensor [5], liquid sensor [6], capacitive pressure sensor [7], temperature sensor [8] and tactile sensor [9], etc. The working mechanism of these sensors is the change of electrical conductivity when they contact with specific materials or deform under applied stress [4,10]. When the distance between nanofillers changes, the varying percolation pathways will affect the electrical conductivity, thus the composites can serve as sensors [10,11]. The liquid sensor

functions based on the swelling phenomena as the liquid enters the polymer network and enlarges the distance between conductive fillers [12]. Some techniques such as melt spinning [13] and compression molding [14], have been reported to fabricate liquid sensors in the form of 1D fiber or 2D film. Melt-processed film of polylactic acid (PLA)/CNT was used as a liquid sensor to compare the liquid sensitivity in various solvents [12,15]. The sizes of sensors are of the order of centimeters which takes up much space and lacks portability. Besides, these techniques require high power consumption. Daniel and coworkers reported 3D printing of PLA/CNT sensors using direct ink writing (DIW) and investigated the effect of printed configurations on liquid sensitivity [6,16]. DIW enables nanocomposites ink to fabricate various structures with only a small amount of materials, without any mold. The sizes of nozzles are of the order of micrometers, which could provide high resolution. These sensors have promising applications to monitor the leakage of solvents in pipelines for security detection [15,16]. However, the ductility of PLA-based nanocomposites was not good enough, thus limiting the deformation of printed structures [16,17]. Besides, the reported nanocomposites sensors could not adapt to

* Corresponding author.

E-mail address: lengjs@hit.edu.cn (J. Leng).

the environment intelligently when the shape of liquid container changed. The single shape of printed sensor limited their application in varying environment. Therefore, it is desired to design and print a new sensor with shape-changing behavior to adapt to the testing environment.

Shape memory polymers (SMPs) are a type of stimuli-responsive smart materials, that have shape-changing capability from temporary shapes to original shapes when triggered by an external stimulus [18–20]. Owing to their intrinsic shape memory properties, SMPs have potential in different applications, such as flexible electronics [21,22], space deployable structures [23,24] and soft robotics [25,26]. Qi and coworkers proposed that the shape of 3D printed SMPs could alter with the change of time under an external stimulus, or called 4D printing [27]. SMP-based 4D shape-changing structures have been printed by fused deposition modeling (FDM) [28], stereolithography (SLA) [29], digital light processing (DLP) [30] and Polyjet [31]. Compared to DIW, these printing methods are usually limited in pure polymers. DIW is much more suitable to print homemade nanocomposites inks with different loadings of nanofillers, and it only requires a small amount of materials [7,32].

Herein, we demonstrate the possibility of a novel 3D and 4D printing of poly(D,L-lactide-co-trimethylene carbonate) (PLMC)/CNT nanocomposites into shape-changing structures. Bao et al. reported electrospun fibrous scaffolds from shape memory PLMC [33]. This material was soft compared to PLA because of the introduction of soft segment of trimethylene carbonate (TMC). We first regulated the rheological and solvent evaporation properties of PLMC/CNT nanocomposites to make it printable. Then we investigated the macroscopic properties of the printed nanocomposites and analyzed its electro-responsive shape-changing capability. To enhance the stiffness and stability, UV photoinitiators were introduced into PLMC/CNT ink to form cross-linking networks under UV light. The modified CNT-based nanocomposites ink with higher gel fraction was used to print shape-changing liquid sensors. The liquid sensors with customer-designed geometries could adapt to changing environments. It revealed the advantages of combining 3D printing with electro-responsive shape-changing performance.

2. Experimental

2.1. Materials

PLMC was purchased from Jinan Daigang Biomaterial Co., Ltd (China). The molar ratio of D,L-lactide(DLLA):TMC was 80:20. The weight-average molecular weight (M_w) and polydispersity index tested by Gel permeation chromatography (GPC) were 420 kDa and 1.9, respectively. Dichloromethane (DCM) and multi-walled carbon nanotubes (CNTs, NC7000) were purchased from Aladdin Industrial Inc and Nanocyl, respectively. PLMC and CNT powders were dried in a vacuum oven at 50 °C for 12 h. The photoinitiators were 2-isopropylthioxanthone (ITX) combined with ethyl 4-dimethylaminobenzoate (EDB), both purchased from Sigma-Aldrich.

2.2. Preparation of CNT-based inks

The ink of PLMC 1/6 was prepared by diluting PLMC pellets in DCM with a weight ratio of 1:5. For PLMC/CNT inks, PLMC was first dispersed in DCM with a weight ratio of 1:20. After diluting, CNTs were dispersed with different concentrations (0.5, 1.0, 1.25, 2.0, 3.0, 5.0, 7.0, 9.0, 10.0, 11.0 wt%) in PLMC. The crosslinking-PLMC (c-PLMC) ink was prepared by diluting ITX/EDB/PLMC/DCM at a weight ratio of 0.01:0.03:1:20. For c-PLMC/CNT ink, the CNTs were dispersed in c-PLMC at a mass fraction of 10 wt%. The CNT-based

inks were mixed through mechanical stirring in a container which was kept open for DCM evaporation. When the weight ratio of PLMC/DCM reached 1/5, the container was sealed and placed in a ball mill mixer (SamplePrep 8000 M, SPEX) for thorough mixing. Finally, the ink was sonicated in an ultrasonic bath for 30 min.

2.3. 3D printing of CNT-based nanocomposites

The ink was fed into a 3 cm³ syringe fixed inside a robot (I&J2200-4, Finsar) and deposited through a micronozzle. The applied pressure ranging from 1.75 to 3.5 MPa was controlled by a pneumatic apparatus (HP-7X, EFD) to match with the robot velocity. The real-time apparent viscosity of various inks was calculated by the capillary flow analysis [34] and the solvent evaporation rate was calculated from the real-time solvent content [16]. For the ink of c-PLMC and c-PLMC/CNT, the printed structure was further placed in a UV chamber to trigger the photopolymerization to obtain crosslinking networks. The printed scaffold after UV crosslinking was called as c-scaffold.

2.4. Shape memory effect measurement

The shape memory cycle (SMC) was conducted on the films to quantitatively evaluate the shape memory effect using Q800 (TA Instruments) [35,36]. The printed film had a size of 30 × 4 × 0.6 mm³. To prevent the film from slipping, a preload of 0.001 N was set to fix it. The procedures were as follows: (i) The rectangular film was thermally equilibrated at 75 °C for 5 min to obtain the initial strain ($\epsilon_{initial}$) of the Nth cycle. Then it was stretched isothermally to 0.08 MPa under a ramping rate of 0.02 MPa min⁻¹ to record the deformed strain (ϵ_{deform}). (ii) The sample was cooled at a rate of 5 °C min⁻¹ and kept isothermal at 0 °C for 5 min. (iii) The external force was unloaded at a rate of 0.05 N min⁻¹ and the specimen was equilibrated at 0 °C for 5 min to obtain the fixed strain (ϵ_{fix}). (iv) The sample was reheated at a rate of 5 °C min⁻¹ and equilibrated at 75 °C for 10 min. The obtained strain was recorded as the residual strain after recovery ($\epsilon_{recover}$). Thus, the shape fixity ratio (R_f) and the shape recovery ratio (R_r) were calculated as follows:

$$R_f(\%) = \frac{\epsilon_{fix}}{\epsilon_{deform}} \times 100\% \quad (1)$$

$$R_r(\%) = \frac{\epsilon_{deform} - \epsilon_{recover}}{\epsilon_{deform} - \epsilon_{initial}} \times 100\% \quad (2)$$

2.5. Characterization of CNT-based nanocomposites

- (1) The electrical property was measured using four-probe method attached to a digital multimeter (6517B, Keithley). The CNT-based inks were poured into molds and dried at room temperature for 24 h to form films at the size of 25 × 55 × 0.6 mm³. For completely drying, the films were then placed in a ventilated oven at 50 °C for 6 h. The volume conductivity was calculated from the resistance based on the length and the cross-sectional area of the films.
- (2) The static mechanical properties of solvent-cast films were tested using an Instron 5944 Universal Machine equipped with a 2 kN load cell. The films were stretched at a speed of 2 mm min⁻¹ at room temperature.
- (3) The dynamic mechanical analysis (DMA) was performed using Q800 under the tension mode. It was conducted at frequency of 1 Hz, a preload of 0.01 N, amplitude of 20 μm

and a heating rate of $3^{\circ}\text{C min}^{-1}$. The rectangular-shaped sample was cut from the solvent-cast film at the size of $30 \times 4 \times 0.6 \text{ mm}^3$.

- (4) The thermal stabilities of the nanocomposites were characterized by thermogravimetric analysis (TGA) on Mettler-Toledo thermal analysis instrument (TGA/DSC1). The sample was scanned from 25 to 800°C in nitrogen atmosphere, at a rate of $10^{\circ}\text{C min}^{-1}$.
- (5) The FTIR spectrum was characterized by Spectrum Two (PerkinElmer Inc.). The sample was tested in a wavenumber range of $800\text{--}4000 \text{ cm}^{-1}$ at a scanning resolution of 4 cm^{-1} .
- (6) The irradiated films of c-PLMC and c-PLMC/CNT were dissolved in DCM at room temperature for 24 h. The undissolved gel was dried in an oven at 50°C for 12 h. The gel fraction (GF) was calculated as follows [37]:

$$GF = \frac{W_g}{W_0} \times 100\% \quad (3)$$

where W_0 and W_g were the weight of films before and after dissolution, respectively.

2.6. Liquid sensing test

The printed U-shaped c-scaffold could serve as a liquid sensor. The liquid sensitivity was measured by monitoring the electrical resistivity during several immersion/drying cycles. The upper of the sensor was attached to two gold electrical probes with a 10 mm gap while the bottom was immersed in the solvent. The real-time resistance was recorded by a digital multimeter (2400, Keithley) connected with a software. Relative resistance change (RRC) was the ratio of difference value between the original and real-time resistance to the original resistance. The influence of solvents (ethanol, normal saline and acetone) on liquid sensitivity was studied using a 4-layer sensor (immersion/drying time of 120/1800, 120/1800 and 20/1900 s, respectively). The effect of layer thickness (2, 4 and 6 layers) on RRC was investigated in ethanol. RRC of the shape-changing sensor with 4 layers was compared in its original, deformed and recovered shapes.

3. Results and discussion

Fig. 1 illustrates the 3D and 4D printing of shape memory nanocomposites by DIW. In order to fabricate electro-responsive structures, PLMC or c-PLMC served as a matrix with shape-changing capability. CNTs served as conducting fillers to endow the material with electrical response as shown in Fig. 1(a). Once CNTs were mixed with PLMC or c-PLMC in DCM to form printable ink, the customer-designed structures could be constructed through DIW. The printing process was based on fast evaporation of DCM under a suitable applied pressure and robot velocity (Fig. 1(b)). After printing, the electro-responsive shape memory structure could show shape-changing behavior in an electric field (Fig. 1(c)). The UV cross-linking reaction of PLMC with photo-initiators is shown in Fig. 1(d). The printing process is illustrated in Fig. S1.

The inks require appropriate viscosity to flow continuously from the micronozzle and maintain the filamentary morphology. Fig. 2(a) depicts the log-log graph of the process-related apparent viscosity versus shear rate. The inks exhibited a shear-thinning performance, which was essential for DIW. The viscosity presented a slightly increasing trend when the CNT content increased. This was because as the mass content of the ink increased, the modulus increased and thus the shape retention ability was enhanced. The solvent evaporation ability of the ink is critical to complete a fluid-solid transition. Fig. 2(b) shows the real-time solvent content of the printed filament extruded from the micronozzle of $200 \mu\text{m}$. It could be seen that various inks showed similar trend and the introduction of CNT shortened the solvent evaporation time. This was due to the increase of mass fraction of solution, which was consistent with the results of previous literature [38]. The solvent content of 10 wt% CNT ink dropped by 70% within 8 min, facilitating the successful printing of the structures.

The electrical properties of the nanocomposites films were critical to select the appropriate CNT content for application as sensors. The volume conductivity of the PLMC/CNT solvent-cast films with respect to the mass fraction of CNT is shown in Fig. 2(c). A power-law theory was utilized to fit conductivity data

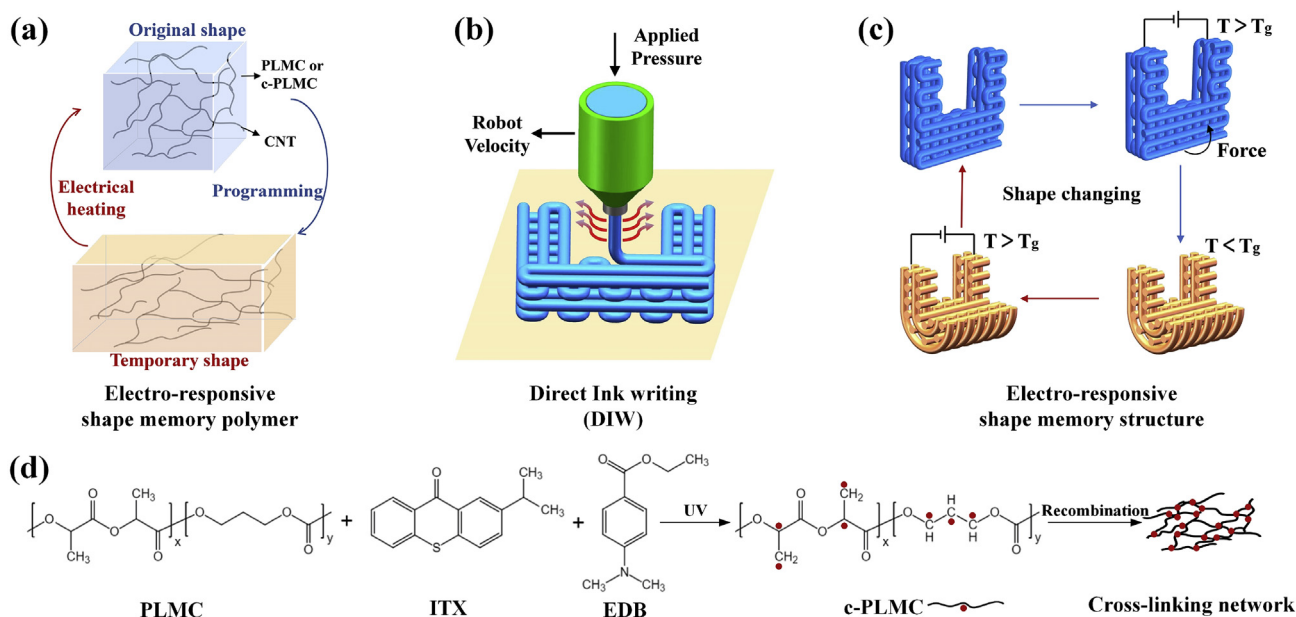


Fig. 1. 3D and 4D printing of shape memory nanocomposites. (a) electro-responsive shape memory behavior of printed material; (b) DIW process; (c) electro-responsive shape-changing behavior of 4D printed structure; (d) UV cross-linking reaction of PLMC to form c-PLMC. (A colour version of this figure can be viewed online.)

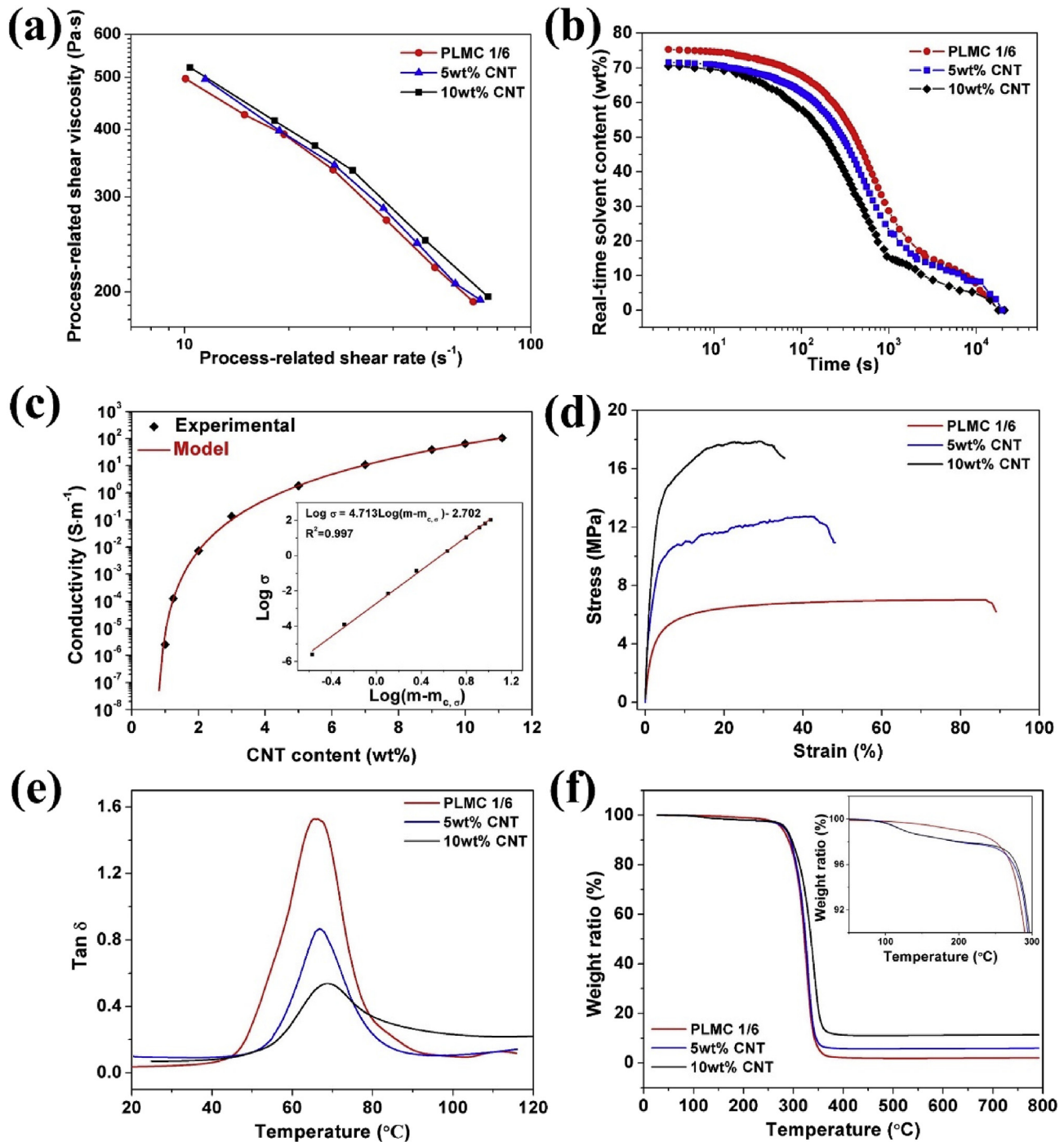


Fig. 2. Investigation of the PLMC/CNT nanocomposites. (a) log-log graph of the process-related apparent viscosity versus shear rate; (b) real-time solvent content as a function of time; (c) electrical conductivity as a function of CNT content. The inset was the log-log fitting curve. Red line is a fit to the experimental data; (d) tensile stress-strain curve of the nanocomposites films; (e) DMA curve of $\tan \delta$; (f) TGA curve. (A colour version of this figure can be viewed online.)

for a percolating network given by [39]:

$$\text{Volume conductivity} = \beta_{c,\sigma} \left(\frac{m - m_{c,\sigma}}{m_{c,\sigma}} \right)^n \quad (4)$$

where m is the CNT loading (wt%), $m_{c,\sigma}$ is the percolation threshold (wt%), $\beta_{c,\sigma}$ and n are the power-law constants. The experimental data agreed well with the fitting curve using Equation (4), yielding the value of $m_{c,\sigma} = 0.73 \pm 0.05$, as shown in Fig. 2(c). The nanocomposites ink of 10 and 11.1 wt% CNT exhibited the electrical

conductivity at 65 and 106 S m⁻¹, respectively. The value was at the same order of magnitude obtained on other similar composite systems containing CNTs and polymers [40,41]. The tensile stress-strain curve of the composites at room temperature is illustrated in Fig. 2(d). It exhibited linear elastic behavior within a small strain range followed by softening behavior, i.e. elasto-plastic behavior. The tensile strength and elastic modulus increased as CNT content increased, while the elongation at break decreased. PLMC showed a low Young's modulus of 190.1 MPa, low tensile strength of 7.0 MPa and high elongation at break of 88.9%. By contrast, nanocomposites

of 10 wt% CNT exhibited a higher Young's modulus of 609.3 MPa, higher tensile strength of ~ 17.9 MPa and lower elongation at break of $\sim 35.4\%$. This was because the addition of CNT limited the mobility of PLMC chains and enhanced the strength.

Fig. 2(e) depicts the DMA curve of $\tan \delta$ under continuous heating. The glass transition temperature (T_g) was defined by the peak of $\tan \delta$ vs. temperature curve, which was essential to trigger shape memory behavior. T_g slightly increased from 66°C (PLMC) to 69°C (10 wt% CNT) because the composites became stiffer thus requiring higher deformed temperature. It could give reference to the reheating temperature in an electric field to trigger shape-changing performance. The thermal stability of the nanocomposites is shown in Fig. 2(f). It could be seen that the composites had an evident thermal decomposition process which corresponded to the cleavage of main chains of PLMC. All the composites decomposed completely above 400°C . The thermal decomposition temperature (T_d) was defined as the temperature with 10% mass loss. From Fig. 2(f), T_d s of PLMC, 5 wt% CNT and 10 wt% CNT were 290 , 294 and 297°C , respectively. The enhancement of T_d resulted from the introduction of CNTs. Considering the composites with 10 wt% CNT showed appropriate viscosity, fast solvent evaporation rate, good conductivity, high mechanical strength, moderate T_g and high thermal stability, we chose this ink for further study.

Various structures were fabricated using 10 wt% CNT ink

extruded from a nozzle of $200\ \mu\text{m}$ as shown in Fig. 3. Fig. 3(a) depicts the side view of 1D filament under the applied pressure of $1.75\ \text{MPa}$ and robot velocity of $0.5\ \text{mm s}^{-1}$. The filament had a uniform diameter of $170\ \mu\text{m}$ and the surface was smooth, providing the basis for printing various structures. Fig. 3(b) shows the zig-zag patterns fabricated under a $1.75\ \text{MPa}$ applied pressure and $0.5\ \text{mm s}^{-1}$ robot velocity. Fig. 3(c) illustrates 2D printed Lily under the applied pressure of $2.1\ \text{MPa}$ and robot velocity of $1\ \text{mm s}^{-1}$. A four-layer scaffold of displaced pattern configuration (DISP) is shown in Fig. 3(d). It was printed using the applied pressure of $2.1\ \text{MPa}$ and robot velocity of $1\ \text{mm s}^{-1}$. The SEM image of DISP scaffold (Fig. 3(e)) featured well-defined structures with pore size $\sim 115 \pm 15\ \mu\text{m}$ and strut width $\sim 174 \pm 11\ \mu\text{m}$. Fig. 3(f) illustrates a 3D printed Dart under $2.8\ \text{MPa}$ and $3\ \text{mm s}^{-1}$. The 3D printed scaffold was used as an electrical component to trigger an LED light under $9\ \text{V}$ (Fig. 3(g)). It was printed under the conditions of $2.1\ \text{MPa}$ and $1\ \text{mm s}^{-1}$. The SEM image of the cut from the scaffold is illustrated in Fig. 3(h), featuring pore size $\sim 329 \pm 22\ \mu\text{m}$ and strut width $\sim 172 \pm 15\ \mu\text{m}$. Fig. 3(i) depicts the micrograph of cross-section of the nanocomposites. It showed that CNTs were dispersed relatively uniformly in the polymer matrix without severe aggregates even at a high mass content of 10 wt%.

The shape memory property of the printed structure was essential to endow the composites with shape-changing behavior. The SMC result of printed nanocomposites containing 10 wt% CNT

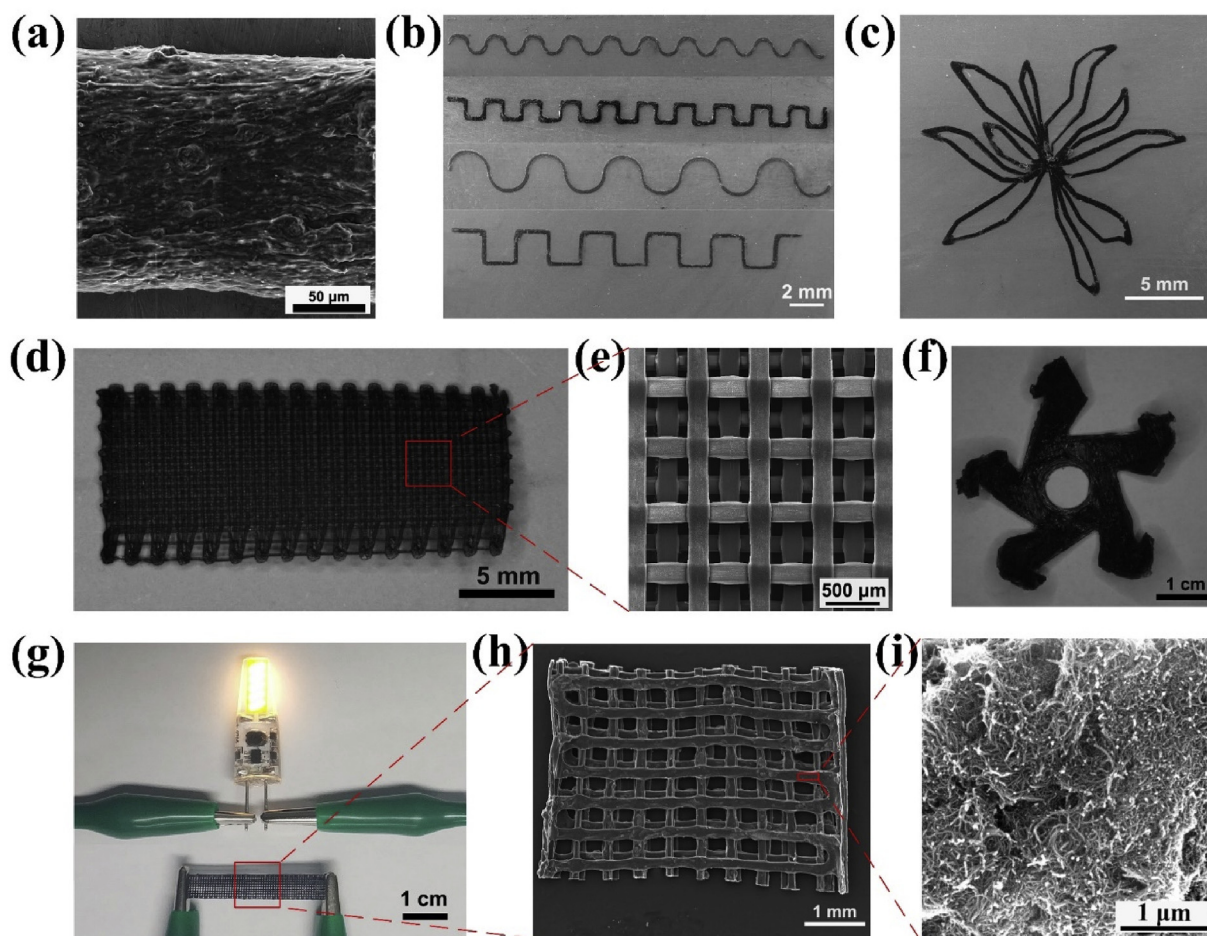


Fig. 3. Various structures printed by 10 wt% CNT ink. (a) side view SEM image of a printed filament; (b) SEM image of zig-zag patterns in 1D array; (c) SEM image of a 2D printed Lily; (d) optical image of a 4-layer scaffold of DISP pattern; (e) SEM enlarged view of the scaffold unit; (f) optical image of a 3D printed Dart; (g) the usage of 3D printed scaffolds as an electrical component; (h) SEM image of the cut electrical component; (i) SEM micrograph of the cross-section of the nanocomposites. (A colour version of this figure can be viewed online.)

is illustrated in Fig. 4(a). Four consecutive SMCs were tested and the shape memory properties calculated by Equations (1) and (2) are illustrated in Fig. 4(b). In all cycles, R_f was nearly 100%, indicating the printed composites had an excellent shape retention ability. While in the first cycle, R_r was only 56.37%. This poor recovery behavior in the initial cycle attributes to the residual stress after printing which is common for SMPs [42]. Repeating several SMCs, R_r increased from 96.31% in the second cycle to 99.99% in the fourth cycle. Both R_f and R_r were close to 100% as shown in Fig. 4(b), exhibiting excellent shape memory behavior and repeatability. The macroscopic shape memory behavior was also demonstrated by a printed scaffold. Firstly, a 5 mm × 5 mm scaffold of 4 layers was printed using 10 wt% CNT ink. A voltage of 25 V was utilized to heat the scaffold and the temperature distribution was recorded with an infrared video (InfraTec GmbH). Fig. S2 shows that under a 25 V electric field, the scaffold could be heated above 80 °C within 47 s. It revealed that it had good Joule heating effect, which created the conditions for realizing electro-responsive shape-changing behavior. To prove it, the composites ink was printed into a U-shaped scaffold as the original shape (Fig. 4(c)). Then it was manually deformed into a temporary folded shape as shown in the SEM image in Fig. 4(d). Fig. 4(d) and Video S1 show the shape recovery process from the folded scaffold to the flat status within 16 s under 25 V. In the first 4 s, it had a high speed of deformation, followed by slowly recovery. It revealed that exposed in an electric field, the printed object could show shape-changing behavior since CNTs generated heat to reach the actuation temperature.

Supplementary data related to this article can be found at <https://doi.org/10.1016/j.carbon.2019.08.047>.

The FTIR spectra of PLMC, c-PLMC and c-PLMC/CNT are shown in Fig. 5(a). PLMC had the characteristic C=O vibration peak at 1745 cm⁻¹, C–O stretching peak at 1080 cm⁻¹ and C–C stretching peak at 1183 cm⁻¹. For c-PLMC, the intensity of –CH– vibration peak at 1317 cm⁻¹, –CH₂– peak at 2920 and 2850 cm⁻¹, and –CH₃ peak at 1453 and 1381 cm⁻¹ attenuated. This was due to the hydrogen abstraction of PLMC by ITX and EDB under UV irradiation. It revealed that the radicals of PLMC molecular chains recombined to form covalent crosslinking networks. This was also evidenced by the GF result (Fig. 5(b)). No GF calculated from Equation (3) was found for PLMC because it was dissolved completely in DCM. After UV crosslinking, GF of c-PLMC and c-PLMC/CNT increased to 27.5 and 18.6%, respectively. The increasing value reflected that with the addition of photoinitiators, the crosslinking networks (c-PLMC) formed under UV light. A decreasing value of GF was seen for the composites because CNTs affected the UV absorption of PLMC. Besides, the existence of CNTs hindered the contact of free radicals initiated by UV light thus decreasing the irradiation efficiency [43]. Therefore, the degree of crosslinking of the composites was lower than c-PLMC.

As shown in Fig. 5(c), T_g decreased from 66 to 55 °C after UV crosslinking due to the introduction of small molecules of ITX and EDB. These small molecules served as plasticizers to enhance the flexibility of molecular chains thus decreasing the transition temperature. T_g of c-PLMC/CNT increased to 57 °C because CNT enhanced the stiffness of the material. Fig. 5(d) shows the storage modulus as a function of temperature and it had two platforms. One was high storage modulus at low temperature and the other was low modulus at high temperature. The variation spanned over

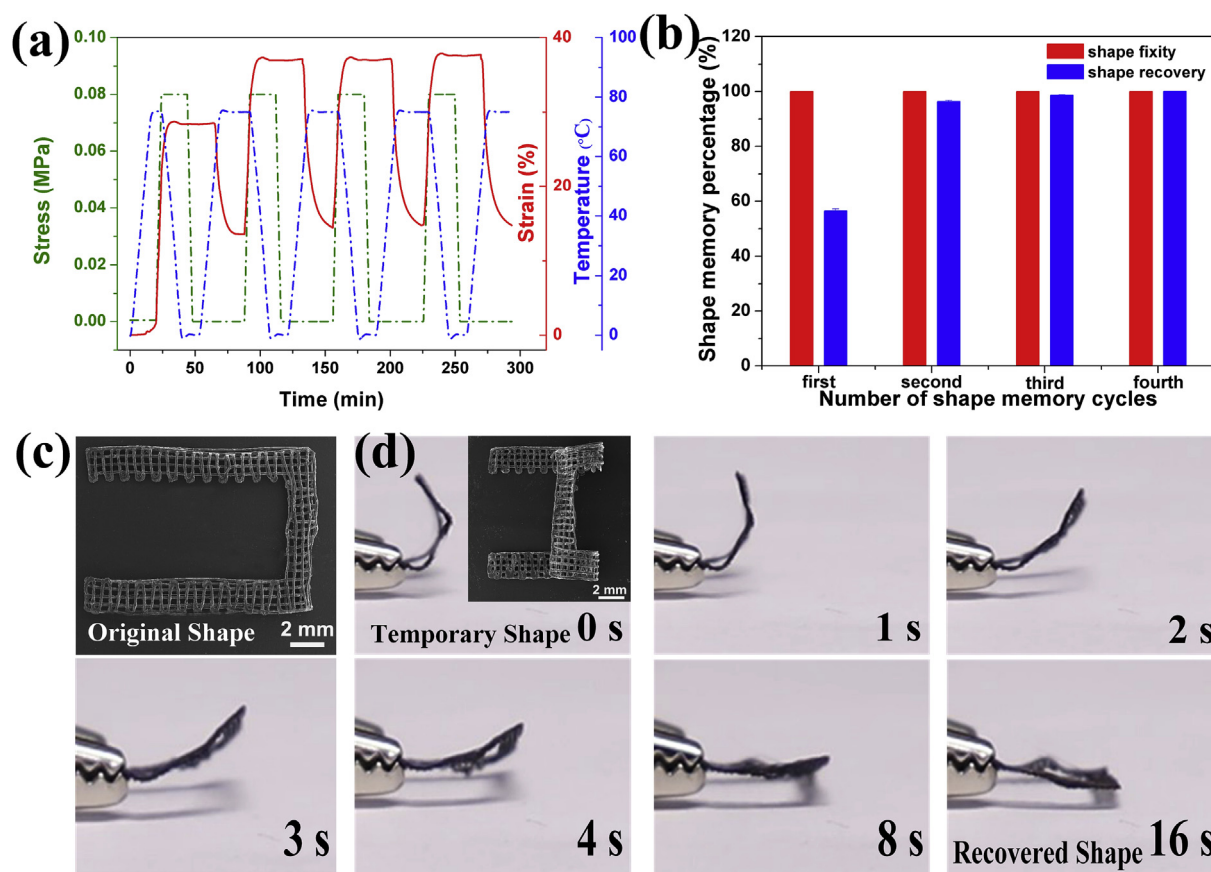


Fig. 4. Shape memory behavior of the printed 10 wt% CNT nanocomposites. (a) four consecutive SMCs; (b) quantitative shape memory properties; (c) original shape of the printed scaffold; (d) shape recovery process of the folded scaffold under a voltage of 25 V. (A colour version of this figure can be viewed online.)

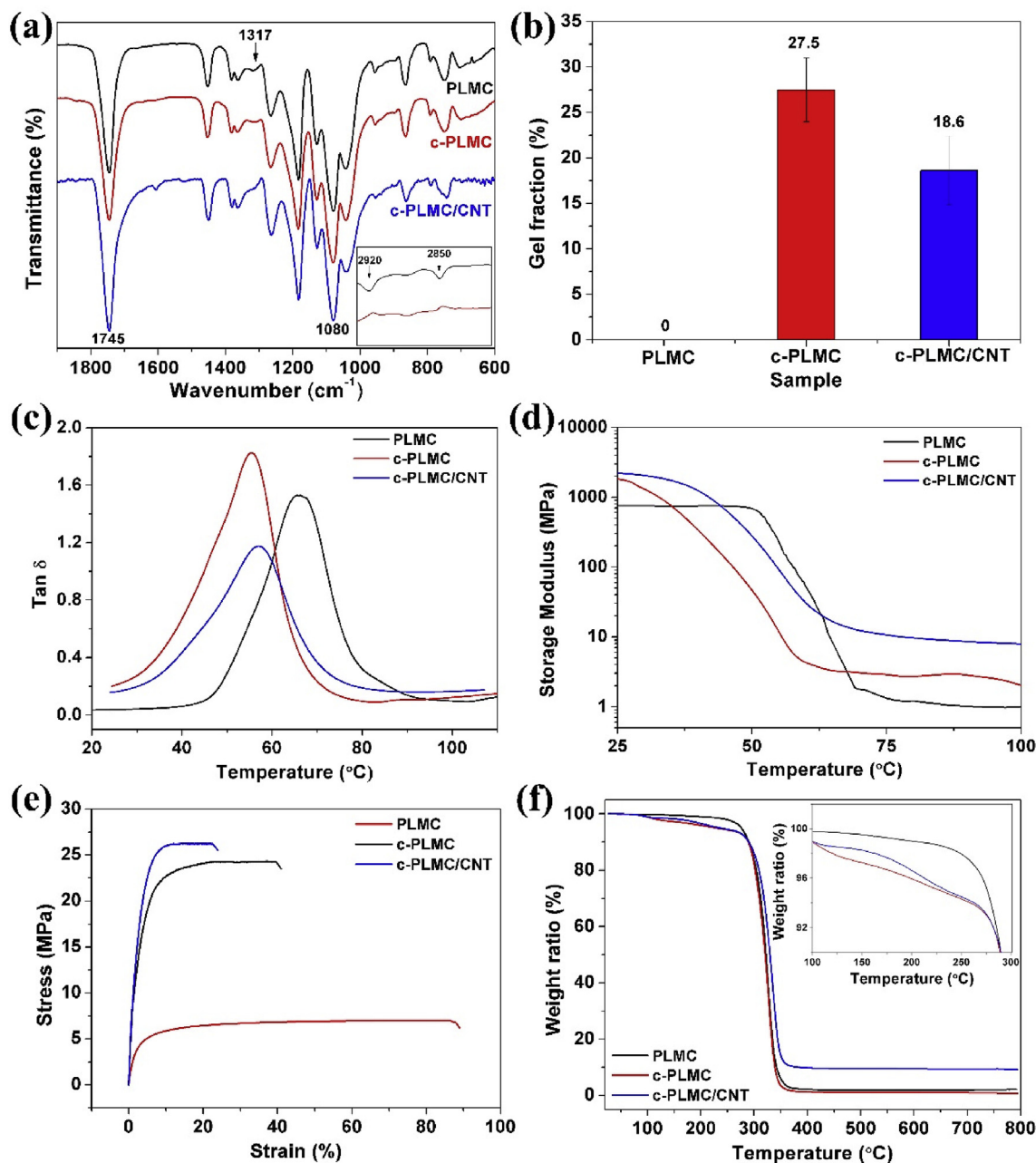


Fig. 5. Investigation of c-PLMC and its nanocomposites after UV crosslinking; (a) FTIR spectrum; (b) GF content; (c) DMA curve of $\tan \delta$; (d) DMA curve of storage modulus; (e) tensile stress-strain curve; (f) TGA curve. (A colour version of this figure can be viewed online.)

three orders of magnitude that contributed to excellent shape memory behavior. The moduli of c-PLMC and c-PLMC/CNT were higher than that of PLMC in both platforms. This enhancement was due to the introduction of crosslinking networks and nanoparticles.

From Fig. 5(e), Young's modulus (870.4 MPa) and tensile strength (24.3 MPa) of c-PLMC increased dramatically after UV crosslinking. The introduction of CNT into c-PLMC enhanced the Young's modulus (1016.8 MPa) and tensile strength (26.2 MPa) in further. However, the increasing amplitude from c-PLMC to c-PLMC/CNT was not as huge as that from PLMC to PLMC/CNT because of the lower degree of crosslinking in the composites. The thermal stability after UV crosslinking is shown in Fig. 5(f). T_{d5} of PLMC, c-PLMC and c-PLMC/CNT were 290, 289 and 290 °C, respectively. It revealed that after crosslinking, the thermal stability was as excellent as the pristine PLMC. The summary and

comparison of the properties are illustrated in Table 1.

To enhance the adaptability in liquid sensing for solvents, the c-scaffold was printed using c-PLMC/CNT. The mechanism of liquid sensing is that RRC would change when the sensor is immersed in solvent. It results from polymer swelling behavior which allows molecules of solvent to penetrate into composites network and disturb connection between CNTs [14]. Flory–Huggins interaction parameter χ_{12} could reflect penetrating ability of solvent into polymer network, which is calculated as follows:

$$\chi_{12} = \frac{V_{sol}(\delta_{pol} - \delta_{sol})^2}{RT} \quad (5)$$

where V_{sol} denotes to the molar volume of solvent, δ_{pol} and δ_{sol} are

Table 1
Characteristics of the polymer and the nanocomposites after UV crosslinking.

Material	GF (%)	aT_g (°C)	bE (MPa)	$c\sigma_m$ (MPa)	$d\epsilon_b$ (%)	eT_d (°C)	Volume conductivity (S m ⁻¹)
PLMC	0	66	190.1 ± 9.2	7.0 ± 0.2	88.9 ± 4.2	290	—
c-PLMC	27.5	55	870.4 ± 17.6	24.3 ± 0.5	41.1 ± 1.7	289	—
PLMC/CNT	0	69	609.3 ± 32.6	17.9 ± 0.8	35.4 ± 1.6	297	65
c-PLMC/CNT	18.6	57	1016.8 ± 30.2	26.2 ± 0.6	24.2 ± 1.2	290	68

^a T_g : glass transition temperature tested by DMA; ^b E : Young's modulus; ^c σ_m : maximum tensile strength; ^d ϵ_b : elongation at break; ^e T_d : decomposition temperature tested by TGA.

Table 2
Characteristics of c-PLMC and solvents used for liquid sensing tests.

Material	δ (MPa ^{1/2})	Boiling point (°C)	Vapor pressure (kPa, 20 °C)	V_{sol} (cm ³ mol ⁻¹)	χ_{12}
c-PLMC	21.62	—	—	—	—
Water	47.47	100	2.34	18	4.85
Ethanol	26.5	78.3	5.80	57.6	0.55
Acetone	19.9	10.0	24.6	74	0.09

solubility parameters of the polymer and the solvent, respectively, R is the ideal gas constant of 8.314 J K⁻¹ mol⁻¹ and T is the absolute temperature. The value of χ_{12} calculated by Equation (5) is illustrated in Table 2, reflecting the interaction of three polymer/solvent pairs. Here, the solubility parameter of c-PLMC was taken the same as PLMC as the approximation [44]. The minimum value (χ_{12} = 0.09) indicated strong interaction, as acetone had the maximum penetrating ability into the polymer. Correspondingly,

we found that it was soluble in acetone. The value for ethanol (χ_{12} = 0.55) was higher than 0.5, indicating ethanol was not a good solvent for c-PLMC. Accordingly, c-PLMC was insoluble but swelled in ethanol. c-PLMC showed the lowest solubility in water as the interaction parameter (χ_{12} = 4.85) was higher than 1.

Based on above theory, we investigated the effect of various solvents on RRC. Fig. 6(a) illustrates the liquid sensitivity of a nanocomposites sensor in three solvents. In every immersion/

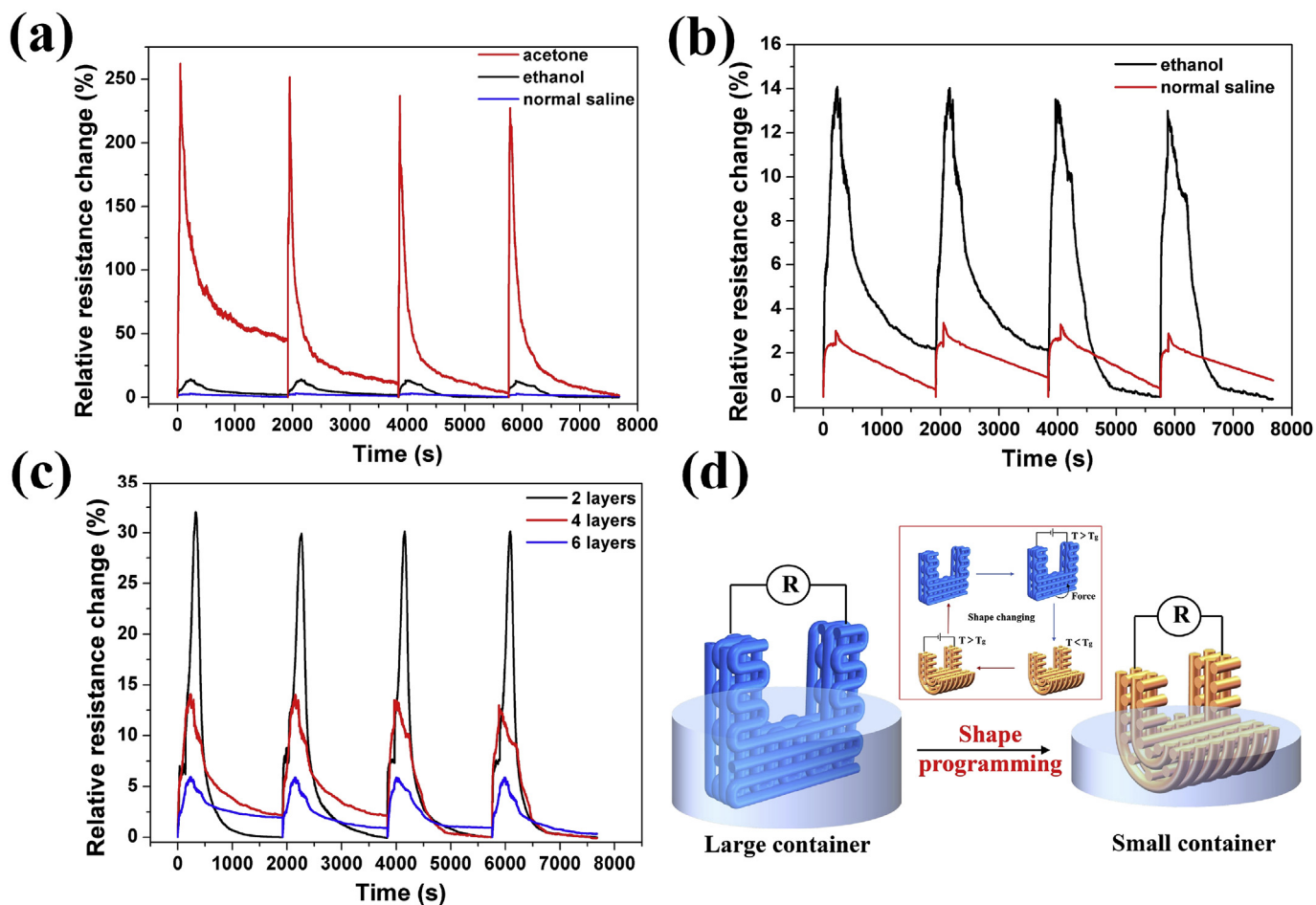


Fig. 6. Liquid sensing capability of the c-scaffold. (a) RRC variation in three solvents during immersion/drying cycles; (b) close-up of RRC in ethanol and normal saline; (c) the effect of layer thickness on RRC; (d) schematic of an electro-responsive shape-changing sensor. (A colour version of this figure can be viewed online.)

drying cycle, RRC dramatically rose up to a maximum peak and then gradually decreased. The initial increase in immersion period was attributed to polymer swelling. In the drying period, plenty of liquid remaining on the sensor started to evaporate, exhibiting a decreasing trend of RRC. The maximum peak of RRC in acetone reached at ~260% in the first cycle and slightly decreased to 240% in the next three cycles. It revealed that the liquid sensitivity became steadier as the number of cycles increased. The maximum RRC value was much higher than that in other solvents. The close-up of RRC is illustrated in Fig. 6(b). In the first cycle, RRC in ethanol and normal saline reached the maximum peaks at 14 and 3%, respectively. The lowest value of RRC in normal saline indicated water had a small impact on polymer swelling. During the drying process, RRC in ethanol decreased sharply while slowly in normal saline. This was because remaining ethanol on the sensor had a higher evaporation speed than water. In the first two cycles in ethanol, RRC did not go back to the initial value after drying. It returned in the next two cycles, indicating the repeatability was enhanced with increasing cycles. Fig. 6(c) shows the influence of layer thickness on RRC when immersed in ethanol. It could be seen RRC peak decreased as layer thickness increased. The sensor with 2 layers showed the highest RRC value above 30% while the sensor with 6 layers exhibited the minimum value of 6%. This was because thicker layers prevented solvent from penetrating and covering the surface of the sensor, leading to a relatively low sensitivity. These results

were consistent with the previous investigation on liquid sensitivity [6]. It revealed that 3D printing could be used to optimize the structural parameters of liquid sensors for high sensitivity.

When liquid level decreases, only small volume of sensor is immersed in liquid, leading to low sensitivity. Designing and printing new sensors for every liquid environment is not convenient and causes waste of materials. Thus, we envision a sensor with shape-changing capability could be deformed to an arbitrary shape to adapt to liquid environment, as illustrated in Fig. 6(d). If the shape of liquid container changes, it only requires a shape memory cycle to endow the sensor with a new shape to adjust to new surroundings. To demonstrate the liquid sensitivity in different environments, the shape-changing sensor was monitored immersed in ethanol and acetone with different liquid levels.

As seen from Fig. 7(a–c), RRC of the deformed and recovered sensor showed the same trend as the original sensor, while RRC peak varied a little due to variation of the immersed volume. Fig. 7(b) shows the RRC peak was at ~16% in the deformed shape, slightly higher than in the original shape. It revealed when the height of liquid level (i.e. the shape of environment) changed, the deformed sensor in folded shape could remain a high value of RRC. This was because the temporary folded shape kept more contact area between sensor and solvent thus increasing the precision of liquid detection. When an electric field was utilized to trigger shape memory behavior, the sensor in folded shape recovered to its

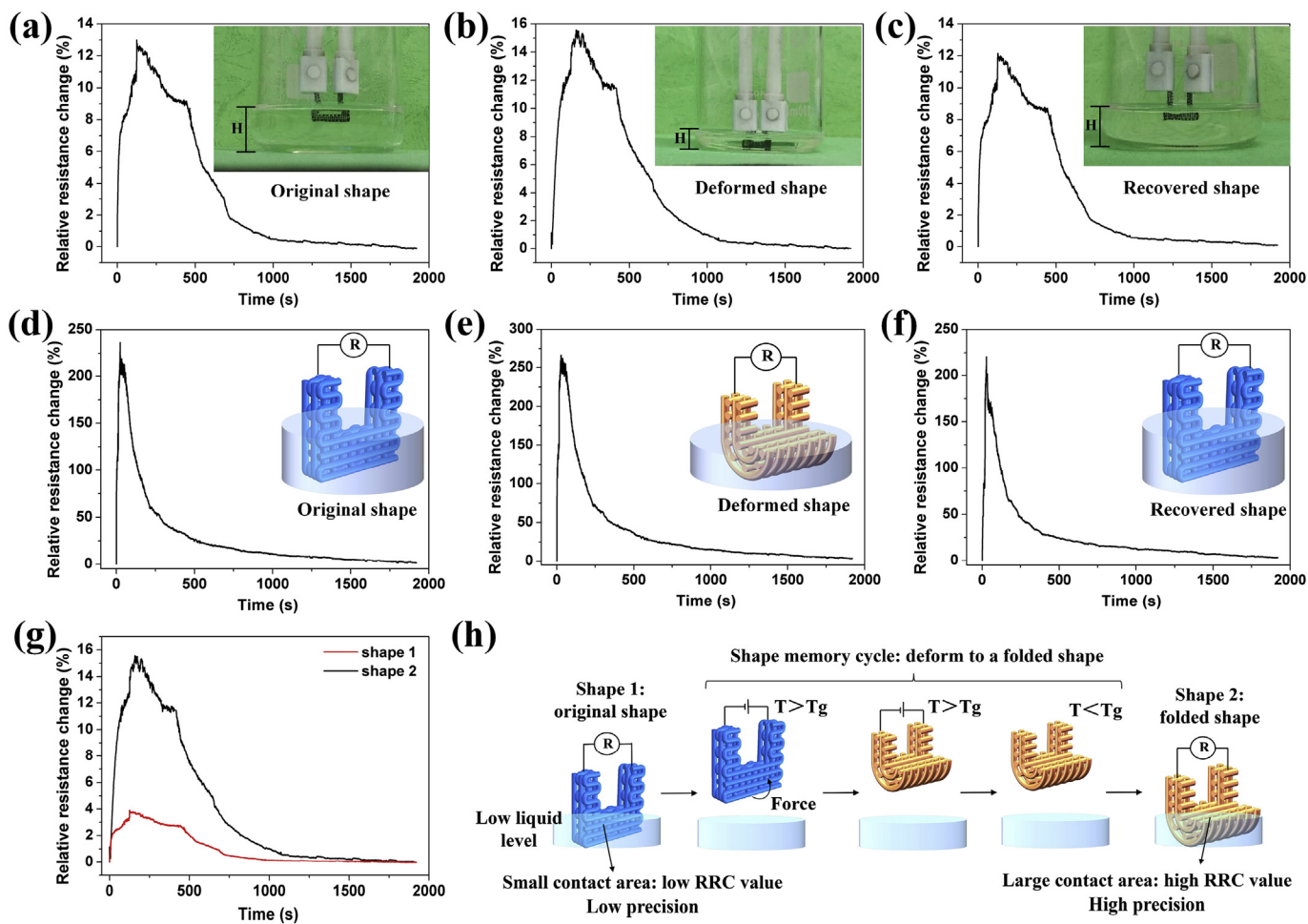


Fig. 7. (a–c) RRC as a function of time in the 4th cycle monitored in ethanol using original, deformed and recovered sensor; (d–f) RRC as a function of time in the 4th cycle monitored in acetone using original, deformed and recovered sensor; (g) comparison of RRC peak in two shapes; (h) schematic for high detecting precision in a folded shape. (A colour version of this figure can be viewed online.)

original shape. The sensor showed excellent repeatability as the RRC peak of recovered sensor (~12%) as depicted in Fig. 7(c) was almost the same as the original one (~13%). The similar detection in acetone also exhibited the same rule as shown in Fig. 7(d–f). We simulated an environment that liquid level decreased. If the sensor was in the static original shape (shape “1”), the contact area between the sensor and solvent would decrease and a low RRC peak of 3.8% was seen (Fig. 7(g)). This was due to weak polymer swelling behavior at very small contact area. To enhance the detection precision in new environment, we utilized an electro-responsive shape memory cycle to change the shape of the sensor. When connected in an electric field, the temperature increased above actuation temperature. As seen from Fig. 5(d), the modulus decreased significantly as the temperature increased, thus the nanocomposites became soft. Then we could easily deform the sensor into shape “2”, a new folded shape. After deformation, the circuit was cut off and the folded shape could be fixed at room temperature. Once immersed in liquid again, the contact area between the folded sensor and liquid increased significantly thus RRC increased fourfold to 15.4%. The whole process for high detecting precision is illustrated in Fig. 7(h). This would help the sensor guarantee high precision for liquid detection. Thus we envision this shape-changing nanocomposites sensor could be extended to adapt to new shapes of surroundings. Besides, the high volume conductivity of the printed sensor with 10 wt% CNTs enabled us to test the resistance change under an applied voltage as low as 6.5 V. It was in the same order of magnitude compared to the previous literature whose mass fraction of CNTs was three times higher than ours [6].

4. Conclusions

In summary, we propose a facile method to construct CNT-based 3D structures with electro-responsive shape-changing capability through direct ink writing. First, we regulate the rheological and solvent evaporation properties to make it printable. We combine electrical conductivity of CNT with shape memory behavior of PLMC. The printed structure exhibit fast electro-responsive shape-changing behavior in a 25 V voltage within 16 s. Then we modified PLMC by hydrogen abstraction reaction using UV photoinitiators to form crosslinking networks. The crosslinking CNT-based nanocomposites enhance the strength and expand the detecting liquid range, thus we print them into liquid sensors. The electro-responsive shape memory behavior endows the sensor with environmental adaptability, as the shape could be redefined to adapt to new environment. The integration of multifunctional CNT-based nanocomposites with shape-changing capability and customer-designed structures, may be of great potential for detecting leakage of various solvents in varying environment. Although we focus on 3D and 4D printing of shape-changing sensors, it could be extended to other electronic applications such as actuators, electromagnetic interference shielding and energy harvesting, etc.

Acknowledgements

This work has been financially supported by the National Natural Science Foundation of China of China (Grant No. 11632005, 11672086), and Foundation for Innovative Research Groups of the National Natural Science Foundation of China under the Grant No. 11421091, for which we are very grateful.

Appendix A. Supplementary data

Supplementary data to this article can be found online at <https://doi.org/10.1016/j.carbon.2019.08.047>.

References

- [1] J. Benson, I. Kovalenko, S. Boukhalfa, D. Lashmore, M. Sanghadasa, G. Yushin, Multifunctional cnt-polymer composites for ultra-tough structural supercapacitors and desalination devices, *Adv. Mater.* 25 (45) (2013) 6625–6632.
- [2] J.H. Kim, S. Lee, M. Wajahat, H. Jeong, W.S. Chang, H.J. Jeong, et al., Three-dimensional printing of highly conductive carbon nanotube micro-architectures with fluid ink, *ACS Nano* 10 (9) (2016) 8879–8887.
- [3] A.E. Jakus, E.B. Secor, A.L. Rutz, S.W. Jordan, M.C. Hersam, R.N. Shah, Three-dimensional printing of high-content graphene scaffolds for electronic and biomedical applications, *ACS Nano* 9 (4) (2015) 4636–4648.
- [4] J.T. Muth, D.M. Vogt, R.L. Truby, Y. Menguc, D.B. Kolesky, R.J. Wood, et al., Embedded 3d printing of strain sensors within highly stretchable elastomers, *Adv. Mater.* 26 (36) (2014) 6307–6312.
- [5] M. Su, F.Y. Li, S.R. Chen, Z.D. Huang, M. Qin, W.B. Li, et al., Nanoparticle based curve arrays for multirecognition flexible electronics, *Adv. Mater.* 28 (7) (2016) 1369–1374.
- [6] K. Chizari, M.A. Daoud, A.R. Ravindran, D. Theriault, 3d printing of highly conductive nanocomposites for the functional optimization of liquid sensors, *Small* 12 (44) (2016) 6076–6082.
- [7] A.D. Valentine, T.A. Busbee, J.W. Boley, J.R. Raney, A. Chortos, A. Kotikian, et al., Hybrid 3d printing of soft electronics, *Adv. Mater.* 29 (40) (2017) 1703817.
- [8] H. Ota, S. Emaminejad, Y.J. Gao, A. Zhao, E. Wu, S. Challa, et al., Application of 3D printing for smart objects with embedded electronic sensors and systems, *Adv. Mater. Technol.* 1 (1) (2016) 1600013.
- [9] S.Z. Guo, K.Y. Qiu, F.B. Meng, S.H. Park, M.C. McAlpine, 3d printed stretchable tactile sensors, *Adv. Mater.* 29 (27) (2017) 1701218.
- [10] N. Hu, Y. Karube, M. Arai, T. Watanabe, C. Yan, Y. Li, et al., Investigation on sensitivity of a polymer/carbon nanotube composite strain sensor, *Carbon* 48 (3) (2010) 680–687.
- [11] E.T. Thostenson, T.W. Chou, Carbon nanotube networks: sensing of distributed strain and damage for life prediction and self healing, *Adv. Mater.* 18 (21) (2006) 2837–2841.
- [12] K. Kobashi, T. Villmow, T. Andres, L. Haussler, P. Poetschke, Investigation of liquid sensing mechanism of poly(lactic acid)/multi-walled carbon nanotube composite films, *Smart Mater. Struct.* 18 (3) (2009), 035008.
- [13] P. Potschke, T. Andres, T. Villmow, S. Pegel, H. Brunig, K. Kobashi, et al., Liquid sensing properties of fibres prepared by melt spinning from poly(lactic acid) containing multi-walled carbon nanotubes, *Compos. Sci. Technol.* 70 (2) (2010) 343–349.
- [14] T. Villmow, A. John, P. Potschke, G. Heinrich, Polymer/carbon nanotube composites for liquid sensing: selectivity against different solvents, *Polymer* 53 (14) (2012) 2908–2918.
- [15] K. Kobashi, T. Villmow, T. Andres, P. Potschke, Liquid sensing of melt-processed poly(lactic acid)/multi-walled carbon nanotube composite films, *Sens. Actuators B Chem.* 134 (2) (2008) 787–795.
- [16] S.Z. Guo, F. Gosselin, N. Guerin, A.M. Lanouette, M.C. Heuzey, D. Theriault, Solvent-cast three-dimensional printing of multifunctional microsystems, *Small* 9 (24) (2013) 4118–4122.
- [17] J.J. Luo, H.B. Wang, D.Q. Zuo, A.P. Ji, Y.W. Liu, Research on the application of mwcnts/pla composite material in the manufacturing of conductive composite products in 3d printing, *Micromachines* 9 (12) (2018) 635.
- [18] M. Behl, A. Lendlein, Shape-memory polymers, *Mater. Today* 10 (4) (2007) 20–28.
- [19] C. Liu, H. Qin, P.T. Mather, Review of progress in shape-memory polymers, *J. Mater. Chem.* 17 (16) (2007) 1543–1558.
- [20] J.S. Leng, X. Lan, Y.J. Liu, S.Y. Du, Shape-memory polymers and their composites: stimulus methods and applications, *Prog. Mater. Sci.* 56 (7) (2011) 1077–1135.
- [21] M. Zarek, M. Layani, I. Cooperstein, E. Sachyani, D. Cohn, S. Magdassi, 3d printing of shape memory polymers for flexible electronic devices, *Adv. Mater.* 28 (22) (2016) 4449–4454.
- [22] R.Y. Liu, X. Kuang, J.N. Deng, Y.C. Wang, A.C. Wang, W.B. Ding, et al., Shape memory polymers for body motion energy harvesting and self-powered mechanosensing, *Adv. Mater.* 30 (8) (2018) 1705195.
- [23] W.M. Sokolowski, S.C. Tan, Advanced self-deployable structures for space applications, *J. Spacecr. Rocket.* 44 (4) (2007) 750–754.
- [24] H.M.C.M. Herath, J.A. Epaarachchi, M.M. Islam, W. Al-Azzawi, J. Leng, F. Zhang, Structural performance and photothermal recovery of carbon fibre reinforced shape memory polymer, *Compos. Sci. Technol.* 167 (2018) 206–214.
- [25] G. Ugur, J.Y. Chang, S.H. Xiang, L.W. Lin, J. Lu, A near-infrared mechano responsive polymer system, *Adv. Mater.* 24 (20) (2012) 2685–2690.
- [26] J. Shintake, V. Cacucciolo, D. Floreano, H. Shea, Soft robotic grippers, *Adv. Mater.* 30 (29) (2018), 1707035.
- [27] Q. Ge, H.J. Qi, M.L. Dunn, Active materials by four-dimension printing, *Appl. Phys. Lett.* 103 (13) (2013) 68–225.
- [28] H. Yang, W.R. Leow, T. Wang, J. Wang, J.C. Yu, K. He, et al., 3d printed photoresponsive devices based on shape memory composites, *Adv. Mater.* 29 (33) (2017), 1701627.
- [29] S.D. Miao, W. Zhu, N.J. Castro, M. Nowicki, X. Zhou, H.T. Cui, et al., 4d printing smart biomedical scaffolds with novel soybean oil epoxidized acrylate, *Sci. Rep.* 6 (2016), 27226.
- [30] D.K. Patel, A.H. Sakhaei, M. Layani, B. Zhang, Q. Ge, S. Magdassi, Highly stretchable and uv curable elastomers for digital light processing based 3d

- printing, *Adv. Mater.* 29 (15) (2017), 1606000.
- [31] Z. Ding, C. Yuan, X.R. Peng, T.J. Wang, H.J. Qi, M.L. Dunn, Direct 4d printing via active composite materials, *Sci. Adv.* 3 (4) (2017), e1602890.
- [32] H.Q. Wei, Q.W. Zhang, Y.T. Yao, L.W. Liu, Y.J. Liu, J.S. Leng, Direct-write fabrication of 4d active shape-changing structures based on a shape memory polymer and its nanocomposite, *ACS Appl. Mater. Interfaces* 9 (1) (2017) 876–883.
- [33] M. Bao, X.X. Lou, Q.H. Zhou, W. Dong, H.H. Yuan, Y.Z. Zhang, Electrospun biomimetic fibrous scaffold from shape memory polymer of pdlla-co-tmc for bone tissue engineering, *ACS Appl. Mater. Interfaces* 6 (4) (2014) 2611–2621.
- [34] S.Z. Guo, M.C. Heuzey, D. Therriault, Properties of polylactide inks for solvent-cast printing of three-dimensional freeform microstructures, *Langmuir* 30 (4) (2014) 1142–1150.
- [35] R. Dolog, R.A. Weiss, Shape memory behavior of a polyethylene-based carboxylate ionomer, *Macromolecules* 46 (19) (2013) 7845–7852.
- [36] T. Xie, Tunable polymer multi-shape memory effect, *Nature* 464 (7286) (2010) 267–270.
- [37] G.H. Koo, J. Jang, Preparation of melting-free poly(lactic acid) by amorphous and crystal crosslinking under uv irradiation, *J. Appl. Polym. Sci.* 127 (6) (2013) 4515–4523.
- [38] H. Wei, X. Cauchy, I.O. Navas, Y. Abderrafai, K. Chizari, U. Sundararaj, et al., Direct 3d printing of hybrid nanofiber-based nanocomposites for highly conductive and shape memory applications, *ACS Appl. Mater. Interfaces* 11 (27) (2019) 24523–24532.
- [39] S. Abbasi, P.J. Carreau, A. Derdouri, M. Moan, Rheological properties and percolation in suspensions of multiwalled carbon nanotubes in polycarbonate, *Rheol. Acta* 48 (9) (2009) 943–959.
- [40] G. Postiglione, G. Natale, G. Griffini, M. Levi, S. Turri, Conductive 3d microstructures by direct 3d printing of polymer/carbon nanotube nanocomposites via liquid deposition modeling, *Compos Part a-Appl S* 76 (2015) 110–114.
- [41] F. Mai, Y. Habibi, J.M. Raquez, P. Dubois, J.F. Feller, T. Peijs, et al., Poly(lactic acid)/carbon nanotube nanocomposites with integrated degradation sensing, *Polymer* 54 (25) (2013) 6818–6823.
- [42] Z.Y. Zhao, F. Peng, K.A. Cavicchi, M. Cakmak, R.A. Weiss, B.D. Vogt, Three-dimensional printed shape memory objects based on an olefin ionomer of zinc-neutralized poly(ethylene-co-emethacrylic acid), *ACS Appl. Mater. Interfaces* 9 (32) (2017) 27239–27249.
- [43] T. Gong, W.B. Li, H.M. Chen, L. Wang, S.J. Shao, S.B. Zhou, Remotely actuated shape memory effect of electrospun composite nanofibers, *Acta Biomater.* 8 (3) (2012) 1248–1259.
- [44] M. Danquah, T. Fujiwara, R.I. Mahato, Self-assembling methoxypoly(ethylene glycol)-b-poly(carbonate-co-l-lactide) block copolymers for drug delivery, *Biomaterials* 31 (8) (2010) 2358–2370.